ACS APPLIED MATERIALS & INTERFACES

www.acsami.org

Research Article

Exchange of Ions across the TiN/TaO_x Interface during Electroformation of TaO_x-Based Resistive Switching Devices

Yuanzhi Ma, David A. Cullen, Jonathan M. Goodwill, Qiyun Xu, Karren L. More, and Marek Skowronski*

Cite This: *ACS Appl. Mater. Interfaces* 2020, 12, 27378–27385

Read Online

ACCESS | Metrics & More | Article Recommendations | Supporting Information

ABSTRACT: The valence change model describes the resistive switching in metal oxide-based devices as due to electroreduction of the oxide and subsequent electromigration of oxygen vacancies. Here, we present cross-sectional X-ray energy-dispersive spectroscopy elemental maps of Ta, O, N, and Ti in electroformed TiN/$TaO_{2.0}$/TiN structures. O, N, and Ti were exchanged between the anode and the functional oxide in devices formed at high power (~1 mW), but the exchange was below the detection limit at low power (<0.5 mW). All structures exhibit a similar Ta-enriched and O-depleted filament formed by the elemental segregation in the functional oxide by the temperature gradient. The elemental interchange is interpreted as due to Fick's diffusion caused by high temperatures in the gap of the filament and is not an essential part of electroformation.

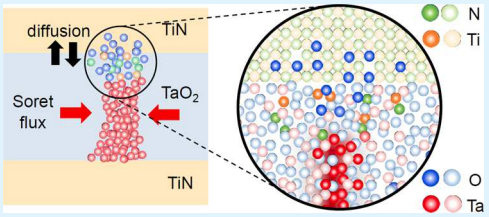

KEYWORDS: *resistive switching devices, valence change model, electroformation, electroreduction, interdiffusion*

Downloaded via CARNEGIE MELLON UNIV on August 7, 2020 at 17:46:54 (UTC).
See https://pubs.acs.org/sharingguidelines for options on how to legitimately share published articles.

1. INTRODUCTION

Metal−insulator−metal resistive switching devices based on transition-metal oxides are of great interest for applications in nonvolatile memories[1,2] and in neuromorphic computing.[3−5] The most promising structures are those based on tantalum and hafnium oxides as they exhibit fast switching, long retention, and high endurance among other properties.[1,6] Currently, work in this field focuses on reduction of energy per switching cycle, improving the endurance, and reducing cycle-to-cycle resistance variability.

The widely accepted basis for the functioning of the TaO_x- and HfO_2-based memory devices is the valence change mechanism (VCM) with its defining characteristics being bipolar switching.[7] Following the work of Jeong et al.,[8] it postulated that initially high device resistance is lowered by the oxygen leaving the functional oxide and entering the anode due to potential difference induced by the applied voltage. Oxygen vacancies generated in the process act as donors in the functional oxide and make it conductive. It is not clear why this process occurs only locally, but it is generally agreed that the result is a small diameter filament that connects the two electrodes. The filament can either be continuous corresponding to the low-resistance state (LRS) of the device or have a gap responsible for the high-resistance state (HRS). Since in the VCM class of devices, the electric field effect dominates the ion motion, the switching is inherently bipolar with SET and RESET occurring in opposite polarities.

The unipolar switching observed, for example, in NiO,[9,10] was explained by the thermochemical mechanism (TCM) that emphasized thermal effects over those of the electric field.[7,11] Electrical conductivity in most oxides is thermally activated, and as-fabricated metal/oxide/metal structures frequently exhibit S-type negative differential resistance (S-NDR) $I-V$ characteristics.[12,13] Such devices are unstable when biased into the NDR region exhibiting threshold switching events and bifurcation of current density into high and low current density domains. This leads to appearance of a small diameter hot spot in the device in which the temperature can easily exceed 1000 K.[14,15] Since at high temperatures, lower oxidation states of metal cations become energetically more stable as evidenced by Ellingham diagram,[16] the appearance of the hot spot should lead to composition change with the high-temperature region becoming metal rich and oxygen poor. Such change can occur by diffusion of metal cations in the direction of temperature gradient or diffusion of oxygen against it. Which one of these two mechanisms dominates remains a matter of dispute.[17−20] Since the temperature gradients associated with current constriction are mostly lateral, the motion of ions is expected to be mostly horizontal rather than vertical (along the electric field direction).

Resistive switching in TaO_x is bipolar,[1] and the structures based on TaO_x were thought to be of VCM-type. Recent experimental results indicate, however, that the distinction between VCM and TCM devices is not as clear as it was initially thought. The TaO_x devices were shown to exhibit

Received: April 17, 2020
Accepted: May 22, 2020
Published: May 22, 2020

© 2020 American Chemical Society

https://dx.doi.org/10.1021/acsami.0c06960
ACS Appl. Mater. Interfaces 2020, 12, 27378−27385

attributes typically associated with the TCM mechanism such as threshold switching and formation of the hot spot before the permanent changes of $I-V$.[12,14,15] In addition, Ta ions are mobile,[21] possibly accounting for a higher fraction of composition change in the electroformation process than the motion of oxygen.[19,20] Scanning transmission electron microscopy (STEM) revealed that Ta ions move in some structures laterally driven by the temperature gradient and vertically along the field direction.[19,20] The STEM data on oxygen distribution so far were not as conclusive.

The microscopy results summarized above focused on redistribution of oxygen and tantalum in the functional layer. In contrast, the study presented here deals with the question of exchange of oxygen and other elements between the functional layer and the electrode during the electroformation process in the TaO_x-based device. The elemental maps after electroformation have been collected by X-ray energy-dispersive spectroscopy (XEDS) mode of STEM on cross-sectional samples. General conclusions of the analysis point to much higher importance of thermal effects in VCM-type devices, making them to exhibit characteristics of the TCM model.

2. RESULTS

The electroformation of devices used for elemental mapping was performed with voltage sweep in a circuit consisting of the voltage source, device under test, and on-chip load resistor of approximately 60 kΩ. The load resistor eliminated the rapid increase of current in the circuit with the S-NDR device[22,23] and the device overheating due to the discharge of parasitic capacitances.[24−27] Several nominally identical devices were formed in positive and negative polarities with the forming $I-V$'s of two devices analyzed here in detail, as shown in Figure 1.

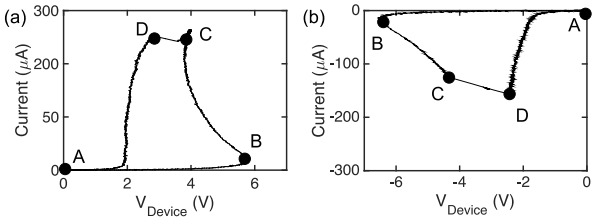

Figure 1. (a) Forming $I-V$ of a device (referred to as device I) under positive bias with R_{LOAD} = 58 kΩ. (b) Forming $I-V$ in negative polarity with R_{LOAD} = 60 kΩ (device II).

One should note that all $I-V$'s are plotted as a function of voltage drop across the device rather than the source voltage. The A→C part of the curve in Figure 1a (device I) corresponds to the S-NDR characteristics of the as-fabricated device. Within NDR, the temperature and current distributions become constricted with the maximum temperature reaching ∼920 K at point C (Supporting Information, Figure S1a). This temperature is high enough for ions to diffuse and form the permanent filament. This process happens in the C → D segment of the characteristics, which represents the time evolution of the device $I-V$ with the source voltage remaining approximately constant. Upon reaching point D, the device is no longer evolving and the segment D to A is the result of downward sweep of the source voltage. Segment D → A is highly nonlinear, sometimes exhibiting a shallow NDR region.[20] A similar shape of $I-V$ after formation was reported in NbO_2[28] devices. Finite element simulation of this segment is included in the Supporting Information as part of the thermal model in Section S2.

Segment D → A is different from HRS of fully formed devices. Full forming requires application of bias with the opposite polarity switching device to LRS.[8] All devices tested exhibited almost identical S-NDR part of $I-V$ and a very similar half-formed $I-V$. However, the point of transition between the two occurred at different current values ranging from 125 to 250 μA. The two $I-V$ traces in Figure 1 correspond to high (device I) and low values of forming current (device II). Other devices formed at intermediate values of current and exhibited changes of elemental distribution between the two extremes. Differences in forming current resulted in differences of dissipated power and the temperature in the device (see Supporting Information, Figure S1 for detail).

Additional insight into the electroformation process is offered by the device in response to a rectangular voltage pulse, as shown in Figure 2. The source voltage pulse with an

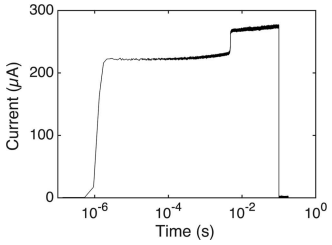

Figure 2. Current transient in response to a constant V_{SOURCE} = 12 V pulse.

amplitude of 12 V was applied at t = 0 s to a device and a load resistor of 37 kΩ. Current remained low for approximately 1 μs corresponding to the incubation time of the threshold switch.[22] The current increase that follows is due to device heating up and evolving along the quasistatic $I-V$ stabilizing close to point C in Figure 1a. The slow changes of current that follow occur on the time scale much longer than the device thermal time constant and are caused by initial stages of composition change due to diffusion driven by the Soret effect.[11,17−20,29−31] It is easy to notice that the composition change in the nascent filament (increase of the [Ta]/[O] ratio) creates a positive feedback loop: the composition change increases the conductivity and current, which in turn increases local temperature and temperature gradient increasing the rate of demixing. This produces a compositional runaway process resulting in a steplike increase of current, collapse of the permanent filament to a diameter much smaller than the initial size of the hot spot, and a significant local temperature increase. The process is akin to thermal runaway and associated current constriction during threshold switching event.[14] The process comes to a steady state when Fick's diffusion flux due to created composition gradient balances the temperature gradient-induced flux.

Figure 3 presents the cross-sectional XEDS elemental maps and the corresponding line profiles of Ta, O, N, and Ti, as well as a reference high-angle annular dark field (HAADF) image of the same area of device I (Figure 1a). The use of large-area X-ray detectors in STEM has increased the XEDS sensitivity to that of the electron energy loss spectroscopy system. The profiles have been obtained by integration of the XEDS signal along the 18 nm wide strip at the position of the filament (red

https://dx.doi.org/10.1021/acsami.0c06960
ACS Appl. Mater. Interfaces 2020, 12, 27378−27385

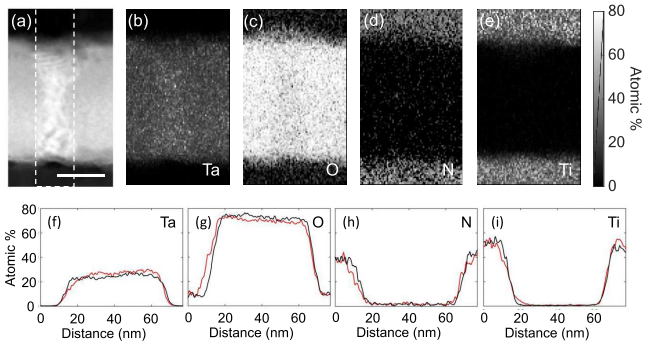

Figure 3. (a) Cross-sectional HAADF image of a filament in device I with forming $I-V$ in Figure 1a. The scale bar corresponds to 20 nm. (b)−(e) Ta, O, N, and Ti elemental maps collected by XEDS from the same location as (a). (f)−(i) Compositional line profiles of Ta, O, N, and Ti corresponding to images (b)−(e). The red trace represents integrated line profiles obtained in the white dashed box in (a), the black trace was integrated over the same width away from the filament. The distance scale starts at the top edge of the image.

line, marked by a white dashed box in Figure 3a) and away from it (black line). The black traces serve here as a reference representing part of the device not affected by high temperatures and current densities. The XEDS signal was not calibrated by standards, and the absolute values of concentrations can deviate from actual values by up to 10 at. %. The relative changes, which are the main subject of this study, however, are correct.

Figure 3b shows the XEDS map of Ta distribution in the proximity of the filament. The slightly brighter contrast in the center of the map indicates a local increase of the Ta content at the location of the filament. A darker area indicating a lower Ta content is visible at the top of the filament next to the interface with the top TiN electrode. One should note that the diameter of the filament (10−20 nm) is much smaller than the thickness of the STEM sample. Accordingly, most of the X-ray photons are generated outside of the filament diminishing the contrast in the image.

The differences of Ta distribution along the filament can be quantitatively assessed in the line profile in Figure 3f. The red line corresponding to the Ta X-ray count in the filament is higher than the black reference curve for most of its length with the exception of 15 nm gap close to the top interface. A local increase of the Ta content is also visible in the lateral line profile obtained in the middle of the functional layer (Supporting Information, Figure S4). Both features are in agreement with the accumulation of Ta in the core of the filament and appearance of the Ta-depleted gap next to the anode observed by HAADF.[20] The Ta signal decreases to zero in both electrodes with no sign of diffusion/electromigration across the interfaces.

The oxygen XEDS map indicates a slight decrease of the oxygen content in the filament column. In addition, a dome-shaped area with a diameter of ∼35 nm and a height of ∼8 nm with an increased oxygen content is visible on top of the filament within the TiN electrode. The composition of the dome was determined to be $TiN_{0.5}O_{0.5}$ (Supporting Information, Section S4). These observations are in agreement with the red line profile in Figure 3g being slightly above the reference trace and lateral line scan (Supporting Information Figure S4a). In proximity of the anode, both traces overlap, and on the TiN side, the red trace is significantly above that of the reference signal. It is important to note that the exchange of oxygen occurs only across the interface with the anode, and there is no corresponding dome at the bottom interface.

Figure 3d,h shows redistribution of nitrogen. In the N map, one can notice a decrease of nitrogen in the area of the oxygen-enriched dome in the top electrode with the corresponding dip in the line profile. The Ti map and the line profile show a decrease of the Ti content in the TiN electrode in proximity of the filament and an increase in the gap area (Figure 3e,i). In both cases, the elemental distributions across the cathode interface are not affected by forming.

Figure 4 shows the set of images and line plots corresponding to those in Figure 3 obtained on a device

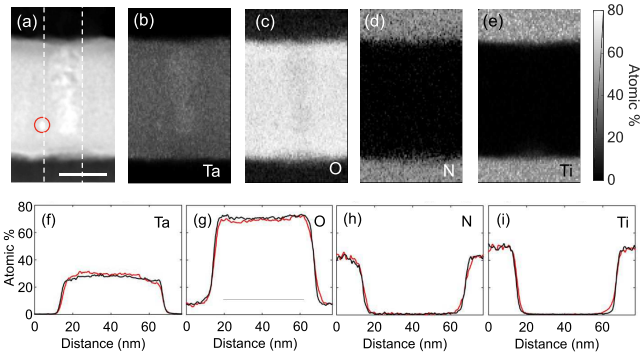

Figure 4. (a) Cross-sectional HAADF image of a filament in device II with forming $I-V$ in Figure 1b. The scale bar corresponds to 20 nm. The feature marked by the red circle is caused by carbon deposition in STEM. (b)−(e) Ta, O, N, and Ti elemental maps collected by XEDS from the same location as (a). (f)−(i) Compositional line profiles of Ta, O, N, and Ti corresponding to images (b)−(e). The line profiles are integrated over the 18 nm wide box marked by white dashed lines in (a). The horizontal axis (distance) starts at the top of each map.

formed in negative polarity at low dissipated power of 380 μW (device II). The HAADF image in Figure 4a shows a contrast associated with the increased Ta content along the length of the filament with the exception of the gap, which in this case is located close to the bottom interface. The same can be seen in the XEDS map (Figure 4b), the line profile along the filament (Figure 4f), and in the lateral line profile (Supporting Information, Figure S4b). All of these findings are consistent with analysis of HAADF data presented elsewhere.[20]

Oxygen concentration in device II decreased slightly in the filament (Figures 4c,g, and S4b) with a marginal increase of density in the gap area. The oxygen concentration drop across the bottom interface appears to be more gradual in the proximity of the filament than in the reference scan. However, there is no discernible oxygen-enriched dome in TiN and the depth of interdiffusion is much shallower than in the sample formed at high current. Ti and N profiles in Figure 4h,i, also show weak signs of interdiffusion at the bottom interface. Overall, the observed changes due to electroformation are consistent with the type of changes observed in device I but are much smaller in extent. This is to be expected if the mechanism is Fick's diffusion as the temperature was much lower. XEDS STEM maps on devices formed at intermediate power levels exhibited similar features (the O-enriched dome in the anode, and interdiffusion of Ti and N in the gap area) as those observed at high power with the extent of changes between those of devices I and II.

https://dx.doi.org/10.1021/acsami.0c06960
ACS Appl. Mater. Interfaces 2020, 12, 27378−27385

Sample configuration used here, i.e., cross-sectional STEM on the location of the filament, allows for mapping relative changes of the filament composition and the ion exchange across interfaces with electrodes, but the contributions to X-ray counts from the material surrounding the filament degrade the signal-to-noise ratio. The elemental distributions deduced from cross sections do not contradict any of the findings based on HAADF and plan-view EELS[20] but are not as precise. For this reason, we have not included quantitative estimates of compositions within the TaO_x layer.

3. DISCUSSION

It is likely that Ti and N exchange across the TiN/TaO_x interface affects the device properties, but it is the exchange of oxygen that is widely thought to be critical for the VCM-type switching. The oxygen ions are thought to cross the interface with the electrode reducing the functional oxide

$$O_O^{\times} \leftrightarrow V_O^{\cdot\cdot} + 2e^- + 1/2O_2\ (\text{gas}) \quad (1)$$

The force that is driving the reaction was asserted to be due to applied bias, which, depending on polarity, can cause transition in either direction.[7,8,32−35] The primary supporting evidence for this interpretation is formation of bubbles at the oxide/anode interface[32,34,36−42] and the presence of the reduced oxide under the deformed electrodes.[34,36,42−44] In a parallel report, we argue that these arguments are flawed as the deformation of electrodes was observed only in circuits relying on current compliance function of the voltage source or using current source.[27] Neither can prevent the current spikes and device overheating, which are not intrinsic to the formation and switching processes. In other words, the reported bubbles and oxide reduction are the experimental artifacts. While we do not claim that electric field-driven exchange does not occur, more evidence needs to be presented to support this mechanism before it can be accepted.

Instead of field-driven oxygen loss, we propose that ion exchange in structures tested here is caused by Fick's diffusion due to concentration gradient. Above results indicate that intermixing is not uniquely associated with oxygen: titanium and nitrogen also cross the interface with the extent of exchange correlated with that of oxygen. Second, while the electric field could induce oxygen motion within the functional oxide or across the interface, it cannot drive the oxygen 10 nm deep into TiN as the electric field in conducting TiN_xO_{1-x} is negligibly small. Third, a brief inspection of the $I-V$ in Figure 1a clearly shows that the device is not formed when the electric field in the device is highest (this corresponds to point B) but at the time when the dissipated power reaches maximum. This is a clear argument for the temperature controlling the electroformation process. Finally, there is a question of an apparent dependence of the exchange on polarity of applied bias, i.e., intermixing occurring at the anode but not the cathode. This observation is in apparent agreement with electric filed-induced exchange of oxygen. The same mechanism could explain motion of Ti ions in opposite direction, i.e., from TiN to oxide, but is in conflict with the exchange of negatively charged nitrogen ions.

Fick's diffusion, instead, offers a natural explanation. It was realized early on that the application of positive bias to the top electrode should create a gap in the filament next to this electrode.[45] High resistivity within the gap causes a voltage drop and creates highest temperatures in the device. This model was confirmed by experimental observation of crystallization at the anode interface.[20]

The temperature distribution in the formed filament was assessed using a simple model similar to that proposed by Larentis et al.[45] (Figure 5a,b). The filament was assumed to be

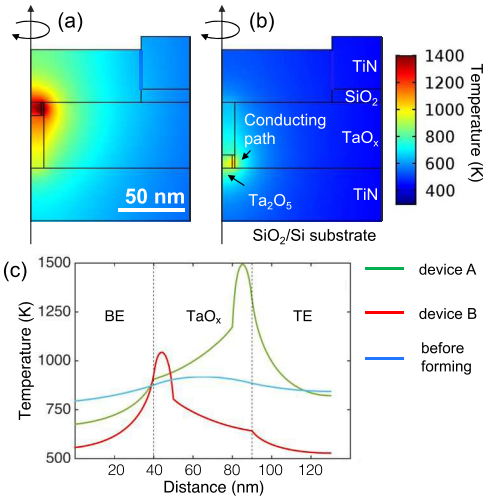

Figure 5. Simulated axisymmetric cross-sectional temperature distribution of devices assuming that a 20 nm wide filament is formed with a 16 nm wide gap on the (a) top (at power dissipation 750 μW) and (b) bottom (at power dissipation 390 μW). The 2 nm thick path conducts current since the gap is made of Ta_2O_5. The views in (a) and (b) show only the magnified portion of the entire structure with an efficient heat sink (see the Supporting Information for more details). (c) Temperature line profiles of positively (green) and negatively (red) formed devices along the vertical direction 9 nm away from the rotational axis (through the conductive path) at the power dissipation of 750 and 390 μW, respectively. The blue curve is the temperature line profile along the center of the device before the formation of the filament (point C of Figure 1a).

a cylinder with a diameter of 20 nm and a temperature-independent conductivity of 10^6 S/m. The diameter is larger than what was observed in the experiments to simplify the geometry. This does not affect the $I-V$ behavior or the temperature distribution in the structure. In the gap region, the filament contains an insulating plug with a diameter of 18 nm consisting of Ta_2O_5 where the conductivity was assumed to be 0. The plug leaves a thin layer of the conducting material around its periphery. This geometry reflects the shape of the filament observed in the cross-sectional TEM with the plug corresponding to the Ta_2O_5 crystallite and the narrow channel representing the conducting subfilaments.[20] The conductivity of the channel was assumed to be of Poole−Frenkel-type with an activation energy of 0.12 eV and a pre-exponential factor of 6×10^3 S/m. Such conductivity reproduced $I-V$ shape of half-formed devices in Figure 1. The details of the simulation procedure are described in Supporting Information, Section S2. Assuming Poole−Frenkel-type conductivity throughout the entire gap (no plug and no channel) while matching the resistance of the device produced qualitatively similar absolute temperatures and temperature distributions.

Figure 5 shows the simulated temperature distribution within the filament and the gap after forming in devices I and II at experimental power values. The temperatures at the anode interface for the two devices are 1310 and 920 K with the corresponding temperatures near cathode of 900 and 645 K.

https://dx.doi.org/10.1021/acsami.0c06960
ACS Appl. Mater. Interfaces 2020, 12, 27378−27385

The activation energy of oxygen diffusion in TiN[46] gives the ratio of diffusion coefficients at 1310 and 900 K of about 1000 or the diffusion length ratio of 30. Since the depth of oxygen interdiffusion near the anode in Figure 2 was about 10 nm, the corresponding depth at ∼900 K would be 0.3 nm and practically undetectable. This explains the lack of interdiffusion across the interface with the cathode in both devices and across the anode interface at low power. Similar arguments can be used to eliminate the interpretation of interdiffusion as occurring during threshold switching. The calculated temperatures (blue trace in Figure 5c) are too low, and their lateral extent (Figure S1) is too large. In summary, the oxygen-rich dome in the anode was created after the filament formation and is its result rather than the origin.

One could consider the case in which the field-induced amount of oxygen loss to the electrode is small, too small to be detected by microscopy methods, but large enough to allow for current flow, Joule heating, and electroformation. This also appears to be unlikely. Recent conductivity measurements of substoichiometric TaO_x films indicate that the compositions that can produce significant current densities and Joule heating in the filament at typical applied voltage values are close to 1:1, i.e., composition of TaO.[47,48]

A direct consequence of exchange being due to Fick's diffusion rather than the electric field is the irreversibility of the process. Many publications on resistive switching assume that the electrodes serve as a reservoir of oxygen, which can be stored or released from the electrode upon application of the electric field depending on polarity.[32,33,35,49] In the TaO_x/TiN system, oxygen, even if present in the anode, cannot go back to the functional layer. The energetics of the exchange is likely to be different in other systems but in all of the entropy of the intermixed state would make the motion back into the oxide difficult. One should also remember that the electric field in metallic electrodes is too low to drive the ion motion. All of these indicate that during the lifespan of a device, the filament will continue to lose oxygen gradually changing switching $I-V$ characteristics. Eventually this could make the filament too conductive to reset inducing failure. Likewise, the diffusion of Ti into the Ta-rich filament is also of concern and should be properly controlled.

Similarly, the finding that Ta and O maps within the functional layer in devices I and II are similar while there is a large difference in the amount of oxygen loss to the electrode indicates that oxygen exchange is not needed for forming and switching. Ta enrichment is clearly due to lateral motion due to the Soret effect following appearance of the hot spot due to threshold switching. Oxygen can also be inferred to redistribute in the TaO_x layer (either laterally or vertically) in structures formed at low temperatures without the need of loss to the electrodes. The above arguments are in direct opposition to the vital element of the VCM model: loss of oxygen to electrodes and its electric field-induced nature.

Vast majority of papers on resistive switching associates the composition changes with oxygen motion alone and considers Ta ions to be immobile. We would like to re-examine this assertion. The most precise estimate of the ion motion was provided by the HAADF and EELS images obtained on plan-view samples.[20] A local increase of Ta density was by a factor of 1.8 with oxygen decreasing by a factor of 0.6 compared to the starting layer composition of TaO_2. This corresponds to approximately the same number of both types of atoms moving in or out of the filament volume, indicating that the diffusion coefficients are similar. The experimental data on diffusion in the Ta−O system are scarce. A recent study of polycrystalline stoichiometric Ta_2O_5 determined the activation energy for oxygen diffusion at 1.6 eV and that of niobium at 3.6 eV (niobium was used *in lieu* of Ta, which does not have a convenient isotope to be used as a tracer).[50] The absolute values of the cation diffusion coefficient were several orders of magnitude lower than that of oxygen. These results are in agreement with the values of 1.6 and 3.7 eV calculated for crystalline λ-Ta_2O_5.[51] These data are in conflict with that obtained on amorphous anodic tantalum oxide. Radiotracer experiments estimated the ratio of the oxygen to tantalum diffusion coefficient at 2:1.[52−54] Similarly close were the values calculated for amorphous suboxides: TaO_2, $TaO_{1.5}$, and TaO.[55] In addition, one has to keep in mind that sputtered films used in fabrication of switching devices are not fully dense with the free volume of as much as 20%.[56,57] Given these values, our estimate of comparable contribution of Ta and O to filament formation appears quite reasonable.

XEDS or EELS results have not allowed for estimation of lateral and vertical redistribution of oxygen in the functional layer. Specifically, these techniques could not detect the O-enriched ring around the filament core, which would be expected in the case of lateral motion induced by the temperature gradient. Such rings were reported in X-ray absorption maps and interpreted as due to demixing of TaO_x.[17] The experimental conditions used in this work, however, were very different compared to ours. The rings appeared only after hundreds of switching cycles with the pulse voltage much in excess of the typical switching voltage intentionally selected to exaggerate the changes in the material. Also, the devices were deposited on thin Si_3N_4, which made the heat extraction less efficient resulting in significantly higher temperatures.[58] This makes it unlikely that the lateral segregation of oxygen could occur in well heat sunk devices at low operating power.

The conclusion of oxygen loss to the anode occurring after formation of the filament applies to TiN/TaO_2 and is a consequence of material parameters such as diffusion coefficients, bonding energies, and others. Since many device structures use the easily oxidizable scavenging layer as the anode, the question arises whether these structures behave in the same way. The ease of electroformation of such structures indicates a possibility of electroreduction. Whether it occurs will have to be answered by future experiments.

The last subject to be discussed is the impact of the Soret effect on switching rather than electroforming. Lateral accumulation of Ta is comparable in spatial extent and concentration change to the vertical depletion at the anode. During RESET pulse, which happens under positive bias, both electric field and the temperature are highest in the gap at the interface with the top electrode. The field exerts a downward force on positively charged Ta ions, while the temperature gradient drives them in opposite direction. Evidently, the electromigration overcomes the thermodiffusion producing a gap. However, the effect of the field is in part compensated by the temperature gradient and depletion is not as deep as it would be otherwise. Behavior of oxygen is expected to be similar. During the SET process, both forces act in tandem reinforcing each other and increasing the rate of resistance change. This effect could, in part, be responsible for rapid SET and gradual RESET.[45]

https://dx.doi.org/10.1021/acsami.0c06960
ACS Appl. Mater. Interfaces 2020, 12, 27378−27385

4. CONCLUSIONS

In conclusion, we have used XEDS to map out the distribution of Ta, O, N, and Ti in the electroformed TiN/$TaO_{2.0}$/TiN resistive switching devices. The maps of Ta and O redistribution are in agreement with previously published HAADF data. In addition, XEDS detected exchange of O, N, and Ti ions across the interface with the anode in devices formed with power dissipation approaching 1 mW. At power below 0.5 mW and the same electric field, the exchange was below the detection limit. These results were interpreted as due to Fick's diffusion caused by high temperatures within the gap in the filament. Distribution of Ta and O in the functional layer remained the same, indicating that the loss of oxygen to the anode is not an essential part of forming and switching. The dominant process of filament formation appears to be the Soret effect driving the Ta and, likely, O ions laterally. The above conclusions indicate that the formation and switching processes in what is considered a typical valence change memory system are much like those in the thermochemical memory model. It appears that many of the processes invoked in the original interpretations can take place in switching devices, but their extent varies between different structures, functional materials, and forming and switching procedures. As the result, the forming and switching mechanism can be a combination of the elementary processes changing from structure to structure. Certainly, drawing the same cartoon of a filament as consisting of few oxygen vacancies is not justified.

5. EXPERIMENTAL SECTION

5.1. Fabrication. The devices examined in this report were fabricated by sputtering a blanket 40 nm thick TiN layer on thermal oxide/Si followed by photolithography and dry etching to define the bottom electrode. Patterned TiN was covered by reactively sputtered 50 nm thick TaO_x and 10 nm SiO_x blanket layers. The active area of the device was defined by e-beam lithography and dry etching of a 150 × 150 nm^2 via in the SiO_x. The stack was finished by sputtering the 40 nm thick TiN top electrode layer and lift-off. The composition of the as-deposited TaO_x was determined to be $TaO_{2.0}$.[20]

5.2. Device Simulation. The device physics was simulated using Comsol Multiphysics, which is a finite element simulation software package. The device temperature, current flow, and conductivity, etc. were simulated by solving two coupled equations describing heat and current flow, and the device was assumed to be connected to a voltage supply and a load resistance in series. Details including the geometry and the material properties can be found in the Supporting Information.

5.3. Material Characterization. STEM lamellae were lifted out using a Ga-ion focused ion beam (FIB) FEI Nova 600 system. The cut was positioned using the outline of the active area visible in secondary electron beam images. Fabrication of devices with a uniform thickness of the functional layer deposited on the flat bottom electrode resulted in the filament forming in the center of the device. Since the active area was only 150 × 150 nm^2, the initial thin section of about 100 nm contained most of the device volume and always contained the filament. The depth of the filament at this point was assessed by tilting the sample in TEM followed by final thinning in FIB.

The STEM images shown in this report were collected by FEI Talos F200X S/TEM operating at 200 keV. The HAADF-STEM images were collected using the Fischione Model 3000 HAADF detector in the system at the collection angle of 76.7−200 mrad. The XEDS images were collected using the "SuperX" energy-dispersive X-ray detector with the probe current of 1 nA.

ASSOCIATED CONTENT

Supporting Information

The Supporting Information is available free of charge at https://pubs.acs.org/doi/10.1021/acsami.0c06960.

Simulated temperature maps in as-fabricated and electroformed devices and detailed description of simulation procedures; additional microscopy data in the form of lateral composition line scans and quantitative estimates of compositions are provided (PDF)

AUTHOR INFORMATION

Corresponding Author

Marek Skowronski − *Department of Materials Science and Engineering, Carnegie Mellon University, Pittsburgh, Pennsylvania 15213, United States;* orcid.org/0000-0002-2087-0068; Email: mareks@cmu.edu

Authors

Yuanzhi Ma − *Department of Materials Science and Engineering, Carnegie Mellon University, Pittsburgh, Pennsylvania 15213, United States;* orcid.org/0000-0002-9901-7659

David A. Cullen − *Center for Nanophase Materials Sciences, Oak Ridge National Laboratory, Oak Ridge, Tennessee 37831, United States;* orcid.org/0000-0002-2593-7866

Jonathan M. Goodwill − *Department of Materials Science and Engineering, Carnegie Mellon University, Pittsburgh, Pennsylvania 15213, United States;* orcid.org/0000-0002-3466-3350

Qiyun Xu − *Department of Materials Science and Engineering, Carnegie Mellon University, Pittsburgh, Pennsylvania 15213, United States*

Karren L. More − *Center for Nanophase Materials Sciences, Oak Ridge National Laboratory, Oak Ridge, Tennessee 37831, United States*

Complete contact information is available at: https://pubs.acs.org/10.1021/acsami.0c06960

Author Contributions

Y.M. designed the experiments, tested the devices, prepared the TEM samples, conducted the microscopy experiments, and contributed to the interpretation and writing of the manuscript. J.M.G. designed and fabricated the devices, D.A.C. and K.L.M. participated in the microscopy experiments and their interpretation. Q.X. participated in preparing the TEM samples. M.S. designed the overall concept of experiments and simulations and contributed toward writing of the manuscript.

Notes

The authors declare no competing financial interest.

ACKNOWLEDGMENTS

This work was supported in part by NSF Grant DMR-1905648 and the Data Storage Systems Center at Carnegie Mellon University. The authors acknowledge the use of the Materials Characterization Facility at Carnegie Mellon University supported by grant MCF-677785 and the electron microscopy facilities at Oak Ridge National Laboratory's Center for Nanophase Materials Sciences, which is a U.S. Department of Energy, Office of Science User Facility.

REFERENCES

(1) Lee, M. J.; Lee, C. B.; Lee, D.; Lee, S. R.; Chang, M.; Hur, J. H.; Kim, Y. B.; Kim, C. J.; Seo, D. H.; Seo, S.; Chung, U. I.; Yoo, I. K.; Kim, K. A. Fast, High-Endurance and Scalable Non-Volatile Memory Device Made from Asymmetric Ta_2O_{5-x}/TaO_{2-x} Bilayer Structures. *Nat. Mater.* **2011**, *10*, 625−630.

(2) Ielmini, D. Resistive Switching Memories Based on Metal Oxides: Mechanisms, Reliability and Scaling. *Semicond. Sci. Technol.* **2016**, *31*, No. 063002.

(3) Ielmini, D. Brain-Inspired Computing with Resistive Switching Memory (RRAM): Devices, Synapses and Neural Networks. *Microelectron. Eng.* **2018**, *190*, 44−53.

(4) Jeong, D. S.; Hwang, C. S. Nonvolatile Memory Materials for Neuromorphic Intelligent Machines. *Adv. Mater.* **2018**, *30*, 1−27.

(5) Burr, G. W.; Shelby, R. M.; Sebastian, A.; Kim, S.; Kim, S.; Sidler, S.; Virwani, K.; Ishii, M.; Narayanan, P.; Fumarola, A.; Sanches, L. L.; Boybat, I.; Le Gallo, M.; Moon, K.; Woo, J.; Hwang, H.; Leblebici, Y. Neuromorphic Computing Using Non-Volatile Memory. *Adv. Phys. X* **2017**, *2*, 89−124.

(6) Chen, Y. Y.; Govoreanu, B.; Goux, L.; Degraeve, R.; Fantini, A.; Kar, G. S.; Wouters, D. J.; Groeseneken, G.; Kittl, J. A.; Jurczak, M.; Altimime, L. Balancing SET/RESET Pulse for > 10^{10} Endurance in HfO_2/Hf 1T1R Bipolar RRAM. *IEEE Trans. Electron Devices* **2012**, *59*, 3243−3249.

(7) Waser, R.; Dittmann, R.; Staikov, G.; Szot, K. Redox-Based Resistive Switching Memories - Nanoionic Mechanisms, Prospects, and Challenges. *Adv. Mater.* **2009**, *21*, 2632−2663.

(8) Jeong, D. S.; Schroeder, H.; Breuer, U.; Waser, R. Characteristic Electroforming Behavior in Pt/TiO_2/Pt Resistive Switching Cells Depending on Atmosphere. *J. Appl. Phys.* **2008**, *104*, No. 123716.

(9) Son, J. Y.; Shin, Y. H. Direct Observation of Conducting Filaments on Resistive Switching of NiO Thin Films. *Appl. Phys. Lett.* **2008**, *92*, No. 222106.

(10) Russo, U.; Ielmini, D.; Cagli, C.; Lacaita, A. L. Self-Accelerated Thermal Dissolution Model for Reset Programming in Unipolar Resistive-Switching Memory (RRAM) Devices. *IEEE Trans. Electron Devices* **2009**, *56*, 193−200.

(11) Ielmini, D.; Bruchhaus, R.; Waser, R. Thermochemical Resistive Switching: Materilas, Mechanisms, and Scaling Projections. *Phase Transitions* **2011**, *84*, 570−602.

(12) Sharma, A. A.; Noman, M.; Abdelmoula, M.; Skowronski, M.; Bain, J. A. Electronic Instabilities Leading to Electroformation of Binary Metal Oxide-Based Resistive Switches. *Adv. Funct. Mater.* **2014**, *24*, 5522−6629.

(13) Gibson, G. A. Designing Negative Differential Resistance Devices Based on Self-Heating. *Adv. Funct. Mater.* **2018**, *28*, 1704175−1704179.

(14) Goodwill, J. M.; Sharma, A. A.; Li, D.; Bain, J. A.; Skowronski, M. Electro-Thermal Model of Threshold Switching in TaO_x-Based Devices. *ACS Appl. Mater. Interfaces* **2017**, *9*, 11704−11710.

(15) Goodwill, J. M.; Ramer, G.; Li, D.; Hoskins, B. D.; Pavlidis, G.; McClelland, J. J.; Centrone, A.; Bain, J. A.; Skowronski, M. Spontaneous Current Constriction in Threshold Switching Devices. *Nat. Commun.* **2019**, *10*, No. 1628.

(16) Schmalzried, H.; Navrotsky, A.*Festkorperthermodynamik*; Verlag Chemie: Weinheim, 1975.

(17) Kumar, S.; Graves, C. E.; Strachan, J. P.; Grafals, E. M.; Kilcoyne, A. L. D.; Tyliszczak, T.; Weker, J. N.; Nishi, Y.; Williams, R. S. Direct Observation of Localized Radial Oxygen Migration in Functioning Tantalum Oxide Memristors. *Adv. Mater.* **2016**, *28*, 2772−2776.

(18) Kumar, S.; Wang, Z.; Huang, X.; Kumari, N.; Davila, N.; Strachan, J. P.; Vine, D.; Kilcoyne, A. L. D.; Nishi, Y.; Williams, R. S. Conduction Channel Formation and Dissolution Due to Oxygen Thermophoresis/Diffusion in Hafnium Oxide Memristors. *ACS Nano* **2016**, *10*, 11205−11210.

(19) Ma, Y.; Li, D.; Herzing, A. A. A.; Cullen, D. A. A.; Sneed, B. T. T.; More, K. L. L.; Nuhfer, N. T. T.; Bain, J. A. A.; Skowronski, M. Formation of the Conducting Filament in TaO_x-Resistive Switching Devices by Thermal-Gradient-Induced Cation Accumulation. *ACS Appl. Mater. Interfaces* **2018**, *10*, 23187−23197.

(20) Ma, Y.; Goodwill, J. M.; Li, D.; Cullen, D. A.; Poplawsky, J. D.; More, K. L.; Bain, J. A.; Skowronski, M. Stable Metallic Enrichment in Conductive Filaments in TaO_x-Based Resistive Switches Arising from Competing Diffusive Fluxes. *Adv. Electron. Mater.* **2019**, No. 1800954.

(21) Wedig, A.; Luebben, M.; Cho, D. Y.; Moors, M.; Skaja, K.; Rana, V.; Hasegawa, T.; Adepalli, K. K.; Yildiz, B.; Waser, R.; Valov, I. Nanoscale Cation Motion in TaO_x, HfO_x and TiO_x Memristive Systems. *Nat. Nanotechnol.* **2016**, *11*, 67−74.

(22) Goodwill, J. M.; Gala, D. K. K.; Bain, J. A. A.; Skowronski, M. Switching Dynamics of TaO_x-Based Threshold Switching Devices. *J. Appl. Phys.* **2018**, *123*, No. 115105.

(23) Goodwill, J. M.; Skowronski, M. Intrinsic Current Overshoot during Thermal-Runaway Threshold Switching Events in TaO_x Devices. *J. Appl. Phys.* **2019**, *126*, No. 035108.

(24) Kinoshita, K.; Tsunoda, K.; Sato, Y.; Noshiro, H.; Yagaki, S.; Aoki, M.; Sugiyama, Y. Reduction in the Reset Current in a Resistive Random Access Memory Consisting of NiO_x Brought about by Reducing a Parasitic Capacitance. *Appl. Phys. Lett.* **2008**, *93*, 33504−33506.

(25) Lu, Y. M.; Noman, M.; Chen, W.; Salvador, P. A.; Bain, J. A.; Skowronski, M. Elimination of High Transient Currents and Electrode Damage during Electroformation of TiO_2-Based Resistive Switching Devices. *J. Phys. D: Appl. Phys.* **2012**, *45*, No. 395101.

(26) Fan, Y. S.; Zhang, L.; Crotti, D.; Witters, T.; Jurczak, M.; Govoreanu, B. Direct Evidence of the Overshoot Suppression in Ta_2O_5-Based Resistive Switching Memory With an Integrated Access Resistor. *IEEE Electron Device Lett.* **2015**, *36*, 1027−1029.

(27) Meng, J.; Zhao, B.; Goodwill, J. M.; Bain, J. A.; Skowronski, M. Temperature Overshoot as the Cause of Physical Changes in Resistive Switching Devices during Electro-Formation. 2020. arXiv preprint arXiv:2004.06571. https://arxiv.org/abs/2004.06571.

(28) Nandi, S. K.; Nath, S. K.; Helou, A. E. l.; Li, S.; Liu, X.; Raad, P. E.; Elliman, R. G. Current Localisation and Redistribution as the Basis of Discontinuous Current Controlled Negative Differential Resistance in NbO_x. *Adv. Funct. Mater.* **2019**, No. 1906731.

(29) Strukov, D. B.; Alibart, F.; Williams, R. S. Thermophoresis/Diffusion as a Plausible Mechanism for Unipolar Resistive Switching in Metal−Oxide−Metal Memristors. *Appl. Phys. A* **2012**, *107*, 509−518.

(30) Arita, M.; Tsurumaki-Fukuchi, A.; Takahashi, Y.; Muraoka, S.; Ito, S.; Yoneda, S. Nanoscale Filaments in Ta-O Resistive RAM Bit Array: Microscopy Analysis and Switching Property. In *2019 IEEE 11th International Memory Workshop (IMW)*; IEEE, 2019; pp 116−119.

(31) Lee, S. H.; Moon, J.; Jeong, Y.; Lee, J.; Li, X.; Wu, H.; Lu, W. D. Quantitative, Dynamic TaO_x Memristor/Resistive Random Access Memory Model. *ACS Appl. Electron. Mater.* **2020**, *2*, 701−709.

(32) Yang, J. J.; Miao, F.; Pickett, M. D.; Ohlberg, D. A. A.; Stewart, D. R.; Lau, C. N.; Williams, R. S. The Mechanism of Electroforming of Metal Oxide Memristive Switches. *Nanotechnology* **2009**, *20*, No. 215201.

(33) Celano, U.; Op De Beeck, J.; Clima, S.; Luebben, M.; Koenraad, P. M.; Goux, L.; Valov, I.; Vandervorst, W. Direct Probing of the Dielectric Scavenging-Layer Interface in Oxide Filamentary-Based Valence Change Memory. *ACS Appl. Mater. Interfaces* **2017**, *9*, 10820−10824.

(34) Mehonic, A.; Buckwell, M.; Montesi, L.; Munde, M. S.; Gao, D.; Hudziak, S.; Chater, R. J.; Fearn, S.; McPhail, D.; Bosman, M.; Shluger, A. L.; Kenyon, A. J. Nanoscale Transformations in Metastable, Amorphous, Silicon-Rich Silica. *Adv. Mater.* **2016**, *28*, 7486−7493.

(35) Cooper, D.; Baeumer, C.; Bernier, N.; Marchewka, A.; La Torre, C.; Dunin-Borkowski, R. E.; Menzel, S.; Waser, R.; Dittmann, R. Anomalous Resistance Hysteresis in Oxide ReRAM: Oxygen Evolution and Reincorporation Revealed by In Situ TEM. *Adv. Mater.* **2017**, *29*, 1700212−1700218.

https://dx.doi.org/10.1021/acsami.0c06960
ACS Appl. Mater. Interfaces 2020, 12, 27378−27385

(36) Buckwell, M.; Montesi, L.; Mehonic, A.; Reza, O.; Garnett, L.; Munde, M.; Hudziak, S.; Kenyon, A. J. Microscopic and Spectroscopic Analysis of the Nature of Conductivity Changes during Resistive Switching in Silicon-Rich Silicon Oxide. *Phys. Status Solidi C* **2015**, *12*, 211−217.
(37) Szot, K.; Speier, W.; Bihlmayer, G.; Waser, R. Switching the Electrical Resistance of Individual Dislocations in Single-Crystalline $SrTiO_3$. *Nat. Mater.* **2006**, *5*, 312−320.
(38) Menke, T.; Meuffels, P.; Dittmann, R.; Szot, K.; Waser, R. Separation of Bulk and Interface Contributions to Electroforming and Resistive Switching Behavior of Epitaxial Fe-Doped $SrTiO_3$. *J. Appl. Phys.* **2009**, *105*, 66104.
(39) Münstermann, R.; Yang, J. J.; Strachan, J. P.; Medeiros-Ribeiro, G.; Dittmann, R.; Waser, R. Morphological and Electrical Changes in TiO_2 Memristive Devices Induced by Electroforming and Switching. *Phys. Status Solidi RRL* **2010**, *4*, 16−18.
(40) Baeumer, C.; Schmitz, C.; Ramadan, A. H. H.; Du, H.; Skaja, K.; Feyer, V.; Muller, P.; Arndt, B.; Jia, C. L.; Mayer, J.; De Souza, R. A.; Schneider, C. M.; Waser, R.; Dittmann, R. Spectromicroscopic Insights for Rational Design of Redox-Based Memristive Devices. *Nat. Commun.* **2015**, *6*, No. 8610.
(41) Dittmann, R.; Muenstermann, R.; Krug, I.; Park, D.; Menke, T.; Mayer, J.; Besmehn, A.; Kronast, F.; Schneider, C. M.; Waser, R. Scaling Potential of Local Redox Processes in Memristive $SrTiO_3$ Thin-Film Devices. *Proc. IEEE* **2012**, *100*, 1979−1990.
(42) Carta, D.; Guttmann, P.; Regoutz, A.; Khiat, A.; Serb, A.; Gupta, I.; Mehonic, A.; Buckwell, M.; Hudziak, S.; Kenyon, A. J.; Prodromakis, T. X-Ray Spectromicroscopy Investigation of Soft and Hard Breakdown in RRAM Devices. *Nanotechnology* **2016**, *27*, No. 345705.
(43) Kwon, D. H.; Kim, K. M.; Jang, J. H.; Jeon, J. M.; Lee, M. H.; Kim, G. H.; Li, X. S.; Park, G. S.; Lee, B.; Han, S.; Kim, M.; Hwang, C. S. Atomic Structure of Conducting Nanofilaments in TiO_2 Resistive Switching Memory. *Nat. Nanotechnol.* **2010**, *5*, 148−153.
(44) Carta, D.; Hitchcock, A. P.; Guttmann, P.; Regoutz, A.; Khiat, A.; Serb, A.; Gupta, I.; Prodromakis, T. Spatially Resolved TiO_x Phases in Switched RRAM Devices Using Soft X-Ray Spectromicroscopy. *Sci. Rep.* **2016**, *6*, No. 21525.
(45) Larentis, S.; Nardi, F.; Balatti, S.; Gilmer, D. C.; Ielmini, D. Resistive Switching by Voltage-Driven Ion Migration in Bipolar RRAM-Part II: Modeling. *IEEE Trans. Electron Devices* **2012**, *59*, 2468−2475.
(46) Desmaison, J.; Lefort, P.; Billy, M. Oxidation of Titanium Nitride in Oxygen: Behavior of $TiN_{0.83}$ and $TiN_{0.79}$ Plates. *Oxid. Met.* **1979**, *13*, 203−222.
(47) Rosário, C. M. M.; Thoner, B.; Schonhals, A.; Menzel, S.; Wuttig, M.; Waser, R.; Sobolev, N. A.; Wouters, D. J. Correlation between the Transport Mechanisms in Conductive Filaments inside Ta_2O_5-Based Resistive Switching Devices and in Substoichiometric TaO_x Thin Films. *Appl. Phys. Lett.* **2018**, *112*, No. 213504.
(48) Rosário, C. M. M.; Thoner, B.; Schonhals, A.; Menzel, S.; Meledin, A.; Barradas, N. P.; Alves, E.; Mayer, J.; Wuttig, M.; Waser, R.; Sobolev, N. A.; Wouters, D. J. Metallic Filamentary Conduction in Valence Change-Based Resistive Switching Devices: The Case of TaO_x Thin Film with $x \sim 1$. *Nanoscale* **2019**, *11*, 16978−16990.
(49) Huang, P.; Liu, X. Y.; Li, W. H.; Deng, Y. X.; Chen, B.; Lu, Y.; Gao, B.; Zeng, L.; Wei, K. L.; Du, G.; Zhang, X.; Kang, J. In *A Physical Based Analytic Model of RRAM Operation for Circuit Simulation*, 2012 IEEE International Electron Devices Meeting (IEDM); IEEE, 2012; pp 26.6.1−26.6.4.
(50) Gries, U. N.; Schraknepper, H.; Skaja, K.; Gunkel, F.; Hoffmann-Eifert, S.; Waser, R.; De Souza, R. A. A SIMS Study of Cation and Anion Diffusion in Tantalum Oxide. *Phys. Chem. Chem. Phys.* **2017**, *20*, 989−996.
(51) Zhu, L.; Zhou, J.; Guo, Z.; Sun, Z. Synergistic Resistive Switching Mechanism of Oxygen Vacancies and Metal Interstitials in Ta_2O_5. *J. Phys. Chem. C* **2016**, *120*, 2456−2463.
(52) Davies, J. A.; Domeij, B.; Pringle, J. P. S.; Brown, F. The Migration of Metal and Oxygen during Anodic Film Formation. *J. Electrochem. Soc.* **1965**, *112*, 675−680.
(53) Whitton, J. L. The Measurement of Ionic Mobilities in the Anodic Oxides of Tantalum and Zirconium by a Precision Sectioning Technique. *J. Electrochem. Soc.* **1968**, *115*, 58−61.
(54) Khalil, N.; L, J. S. L. The Anodic Oxidation of Valve Metals - I.Determination of Ionic Transport Numbers by a-Spectrometry. *Electrochem. Acta* **1986**, *31*, 1279−1285.
(55) Xiao, B.; Yu, X.; Watanabe, S. A Comparative Study on the Diffusion Behaviors of Metal and Oxygen Ions in Metal-Oxide-Based Resistance Switches via Ab Initio Molecular Dynamics Simulations. *ACS Appl. Electron. Mater.* **2019**, *1*, 585−594.
(56) Tsuruoka, T.; Valov, I.; Tappertzhofen, S.; Van Den Hurk, J.; Hasegawa, T.; Waser, R.; Aono, M. Redox Reactions at Cu,Ag/Ta_2O_5 Interfaces and the Effects of Ta_2O_5 Film Density on the Forming Process in Atomic Switch Structures. *Adv. Funct. Mater.* **2015**, *25*, 6374−6381.
(57) Xu, Q.; Ma, Y.; Skowronski, M. Nanoscale Density Variations in Sputtered Amorphous TaOx Functional Layers in Resistive Switching Devices. *J. Appl. Phys.* **2020**, *127*, No. 055107.
(58) Wang, Z.; Kumar, S.; Wong, H. S. P.; Nishi, Y. Effect of Thermal Insulation on the Electrical Characteristics of NbO_x Threshold Switches. *Appl. Phys. Lett.* **2018**, *112*, 73102.

https://dx.doi.org/10.1021/acsami.0c06960
ACS Appl. Mater. Interfaces 2020, 12, 27378−27385